BNL-222814-2022-JAAM

Nanoscale-correlated octahedral rotations in BaZrO3

I. Levin, M. Han

To be published in "PHYSICAL REVIEW B"

December 2021

Condensed Matter Physics and Materials Science Department

Brookhaven National Laboratory

U.S. Department of Energy

USDOE Office of Science (SC), Basic Energy Sciences (BES) (SC-22)

Notice: This manuscript has been authored by employees of Brookhaven Science Associates, LLC under Contract No.DE-SC0012704 with the U.S. Department of Energy. The publisher by accepting the manuscript for publication acknowledges that the United States Government retains a non-exclusive, paid-up, irrevocable, world-wide license to publish or reproduce the published form of this manuscript, or allow others to do so, for United States Government purposes.

DISCLAIMER

This report was prepared as an account of work sponsored by an agency of the United States Government. Neither the United States Government nor any agency thereof, nor any of their employees, nor any of their contractors, subcontractors, or their employees, makes any warranty, express or implied, or assumes any legal liability or responsibility for the accuracy, completeness, or any third party's use or the results of such use of any information, apparatus, product, or process disclosed, or represents that its use would not infringe privately owned rights. Reference herein to any specific commercial product, process, or service by trade name, trademark, manufacturer, or otherwise, does not necessarily constitute or imply its endorsement, recommendation, or favoring by the United States Government or any agency thereof or its contractors or subcontractors. The views and opinions of authors expressed herein do not necessarily state or reflect those of the United States Government or any agency thereof.

Nanoscale-correlated octahedral rotations in $BaZrO_3$

I. Levin, M. G. Han, H. Y. Playford, V. Krayzman, Yimei Zhu and R. A. Maier

[1]Materials Measurement Science Division
National Institute of Standards and Technology Gaithersburg MD 20899
[2]Condensed Matter Physics & Materials Science
Brookhaven National Laboratory Upton, NY 11973
[3]ISIS Facility, Rutherford Appleton Laboratory
Didcot UK

Igor.levin@nist.gov

Abstract

$BaZrO_3$ is reportedly one of few perovskites that retains an ideal cubic structure down to zero Kelvin even though its ground state as predicted by first-principles calculations has remained contentious. Here, we combine electron diffraction with total neutron scattering measured on ceramic samples at cryogenic temperatures to demonstrate that below 80 K, this compound undergoes a structural change associated with the onset of correlated out-of-phase rotations of [ZrO_6] octahedra. The change is manifested in the appearance of weak but relatively sharp superlattice reflections at *½hkl* (*h*, *k*, *l*=odd), which are readily detectable by electron diffraction. Atomistic structural refinements from the total neutron scattering data confirmed that these reflections are associated with octahedral tilting. The observed rotations are consistent with the $a^0a^0c^-$ type and feature a coherence length of about 3 nm. The average structure of $BaZrO_3$, as seen by Bragg diffraction, remains cubic. According to the electron diffraction data, Nb-doped $BaZrO_3$ undergoes a similar structural transition but in this case, the tilting couldn't be recovered from the neutron scattering, suggesting that the distortions are smaller compared to those in the pure compound.

I. Introduction

Barium zirconate, $BaZrO_3$, which crystallizes with the perovskite structure [1], is a widely used component in dielectric and ferroelectric ceramic formulations [2-5]. If doped, it also exhibits promising proton-conduction properties [6] and, as such, is being considered for fuel-cell and hydrogen separation applications [7]. For $BaZrO_3$, the Goldsmith tolerance factor, which characterizes the stability of the perovskite structure to distortions, is close to the ideal value of unity and thus expected to yield an ideal cubic arrangement. Indeed, neutron powder diffraction measurements demonstrated that $BaZrO_3$ retains *Pm-3m* symmetry down to temperatures near absolute zero, a rare case among perovskite-structured compounds [8-10]. Nevertheless, several *ab initio* theoretical calculations suggested the existence of a structural instability associated with octahedral rotations [8, 11-14]. An apparent discrepancy between the computational predictions and experiments has been reconciled by hypothesizing these structural distortions to be correlated only over the local scale, thus remaining undetectable by Bragg diffraction. Zero-point vibrations and degenerate energies for the various structures with anti-phase tilting have been proposed as possible reasons for the lack of long-range order. Yet, a recent study [9] highlighted the sensitivity of computations to the choice of the exchange-correlation functional and concluded with a claim that $BaZrO_3$ retains a cubic ground state, disavowing conclusions of the earlier theoretical work.

The experimental evidence presented thus far either in support or against a symmetry-lowering freezing of octahedral rotations in $BaZrO_3$ has been indecisive. One argument cited in favor of octahedral tilting is a relatively large spread of Ba-O bond lengths as probed by extended X-ray absorption fine structure measurements at room temperature [13]; however, linking this observation and correlations among rotations of individual octahedra is ambiguous. $BaZrO_3$ exhibits prominent Raman spectra despite first-order scattering in cubic perovskites prohibited by symmetry. Recent studies of $BaZrO_3$ single crystals [14] attributed these spectral features to second-order events with no signs of phase transitions down to low temperatures; nevertheless, the authors speculated that such second-order Raman scattering could be linked to some kind of structural disorder. An absence of phase transitions at low temperatures has also been conjectured from inelastic neutron-scattering measurements performed on powder samples [9], which suggested that the energy and width of a feature assumed to represent the R_{25} phonon associated with out-of-phase octahedral rotations remain approximately constant between 500 K and 5 K. However, these analyses relied on several assumptions and fitting of spectral features exhibiting a significant overlap.

Furthermore, the dielectric permittivity of $BaZrO_3$ displays several low-temperature anomalies [8, 15]. That at the lowest temperature of 7 K has been attributed to freezing of local octahedral rotations, whereas those occurring between 11 K and 80 K to defect-related relaxations [8]. All these anomalies disappeared upon substitution of Zr^{4+} (ionic radius R=0.72 Å [16]) by 0.005 Nb^{5+} (R=0.64 Å); this disappearance has been accompanied by a dramatic decrease in dielectric loss. In contrast, acceptor dopants, Y^{3+} (R=0.9 Å) or Ga^{3+} (R=0.62 Å), preserved the 7 K anomaly [15]. The authors noted that given the proposed association of this anomaly with octahedral tilting, its behavior as a function of doping with species of different sizes is surprising [15]. Indeed, from basic crystal-chemical reasoning, the smaller Nb and Ga should suppress the rotations whereas the larger Y is expected to have the opposite effect.

This uncertainty about the detailed structural behavior of $BaZrO_3$ motivated us to perform a study of the local structure in this classic perovskite. We employed electron diffraction at cryogenic temperatures and atomistic structural refinements from neutron total-scattering data to determine the structure of both

pure and Nb-doped (0.5 %) $BaZrO_3$. Electron diffraction in a transmission electron microscope (TEM) permits the analysis of single crystallites in polycrystalline samples and has high sensitivity to short-range ordering because electrons interact strongly with matter. Atomistic large-box refinements from neutron powder total-scattering data enable quantitative insight into the nature of the local and nanoscale atomic order. Indeed, by combining these two approaches, we obtained conclusive evidence for the emergence of octahedral rotations correlated over the nanoscale below 80 K.

II. Experimental

Samples for this study were prepared by solid state synthesis using raw materials and procedures similar to those reported in [15]. $BaCO_3$ (99.99 %), ZrO_2 (99.978 %), and, for the Nb-doped sample $BaZr_{0.995}Nb_{0.005}O_3$, Nb_2O_5 (99.995%) were mixed and ball-milled in isopropanol in a planetary mill using yttria-stabilized zirconia as a grinding media. The dried powders were pelletized and calcined at 1300 °C. After a second ball milling, powders were pelletized and sintered in air at 1500 °C. The Nb-doped powders were more difficult to densify than pure $BaZrO_3$ and therefore, in that case, the pelletization was performed using cold isostatic pressing. X-ray diffraction with $CuK\alpha_1$ radiation was used to confirm phase purity. The off-white color of the doped sample suggests that Nb is present as Nb^{5+} ions, with the excess positive charge (relative to Zr^{4+}) compensated by interstitial oxygen and/or cation vacancies. TEM samples were prepared by mechanical polishing of sintered pellets, followed by ion thinning at -100 °C until perforation. The samples were coated with a thin layer of carbon to improve their electrical conductivity. Electron diffraction experiments were performed in a JEOL ARM 200CF operated at 200 kV. The TEM samples were cooled down to 12 K with a customized double-tilting liquid-helium cooling holder (HCHDT3010, Gatan, Inc.). Neutron scattering measurements were performed in the POLARIS time-of-flight powder diffractometer at ISIS. The samples were placed in vanadium containers, 6 mm in diameter. Temperature control was achieved using a cryostat. Data suitable for Rietveld refinements were collected at a series of temperature between 2 K and 300 K. Total-scattering data, which required significantly longer recording times, were collected at 2 K, 10 K, 15 K, 50 K, and 300 K (a set of low temperatures was selected according to those of the dielectric anomalies). Because of time limitations encountered during variable-temperature measurements, the room-temperature total-scattering data were recollected with both samples placed in a sample changer. We used the latter data to obtain reference values of lattice parameters for the pure and doped compounds because the changer ensures a well-defined and reproducible sample position in the beam. All neutron-scattering data were reduced using the MANTID software package. The total-scattering data were further processed using the GUDRUN software to obtain a scattering function, $S(Q)$, and its Fourier transform, which represents an atomic pair-distribution function (PDF). The differences between the experimental signals of $BaZrO_3$ at 2 K and 50 K, as well as those between $BaZrO_3$ and $BaZr_{0.995}Nb_{0.005}O_3$, are small but significant relative to the statistical noise levels deduced from estimated standard deviations in the measured intensities (Fig. 1).

Rietveld refinements were performed using GSAS [17]. Atomistic structural refinements were carried out via simultaneous fitting of the neutron scattering function, $S(Q)$, its corresponding PDF in the $D(r)$ form, and the Bragg profile using the RMCProfile software [18]. The instrumental resolution function was explicitly accounted for [19, 20]. The weights assigned to the individual datasets and restraints were adjusted automatically during fits using the procedure that is based on statistical analysis of changes in the total residual and its individual components after a series of atomic moves [19].

Instantaneous structures of pure and Nb-doped $BaZrO_3$ were represented with configurations of 20 × 20 × 20 perovskite unit cells, sampling interatomic distances up to ≈40 Å. Given only a small content of Nb in the doped sample, we decided not to include these species explicitly; instead, the neutron scattering length on the Zr sites was adjusted to account for the Nb substitution. In addition to the experimental data, we employed two types of restraints on atomic moves to regularize the refined configurations. In the first type, the so-called polyhedral restraints were imposed on the Zr-O distances and O-Zr-O angles within each [ZrO_6] octahedron to favor more rigid polyhedra [21]. In the second type, developed in this study, constrained coordinates and atomic displacement parameters (ADP) of atomic sites in an asymmetric unit were obtained by folding a refined configuration onto a single unit cell. Two types of ADP constraints were implemented. In the first version, each component of an APD tensor is restrained to match a specified value (e.g., determined from Rietveld refinements), with the strength of this restraint controlled by a weight that determines the contribution of the corresponding penalty function to the total residual. In the second version, numerical values of ADPs are left unconstrained but the relations between the ADP components are forced to obey the specified space-group symmetry within a certain tolerance. The "stiffness" of these criteria can be modified by changing the tolerance values; in this version of constraints, there is no penalty function and all atomic moves that violate the conditions imposed on the ADPs are rejected.

The rotation angles for [ZrO_6] octahedra in refined configurations were determined using both GASP [22], which employs geometric algebra, and the deformation-mode analysis described in [23, Supplemental information]; the latter approach was also used to generate model configurations with pre-defined octahedral tilts for tests involving synthetic data.

Based on prior experience [19], the RMC refinements were continued until at least 500 moves were accepted per atom, despite that only minimal improvements in the residuals were observed at much earlier stages of the fits. We found that such large numbers of moves, which are at least an order of magnitude greater than those typically quoted for RMC refinements, are critical for recovering the correlated rotations; however, these numbers limit the sizes of atomic configurations that can be considered within reasonable times using available computing power.

III. Results and Discussion

Rietveld refinements of average structures

Consistent with previous work, our Rietveld refinements revealed that the contraction of the lattice parameter, *a*, on cooling saturates below ≈50 K (Fig. 2a). For T<100 K, the *a*(T) dependencies for $BaZrO_3$ and $BaZr_{0.995}Nb_{0.005}O_3$ start to diverge, with the doped sample displaying a stronger saturation. The observed flattening of the *a*(T) trend at low temperatures has been shown to be caused by quantum-fluctuation effects [8], which thus appear to become even more significant upon doping with Nb. As is common in perovskites, oxygen motion is found to be strongly anisotropic, with larger displacements perpendicular to the Zr-O bonds (Fig. 2b). The degree of this anisotropy decreases on cooling but remains pronounced down to 2 K. At higher temperatures (including ambient), the ADP of Ba is greater than that of Zr, which is typical for 12- vs. 6-fold coordinated cations, whereas below 100 K, the sign of this difference is reversed (Fig. 2c). The absolute magnitudes of ADPs for all the atoms as well as the anisotropy of displacements for oxygens agree with the results reported by Perrichon *et al* [9 but differ from those quoted by Knight [10], who obtained significantly larger values for the cations and weaker anisotropy for oxygen. Further tests indicated that this discrepancy can be attributed to a more limited

d-spacing range covered by the HRPD instrument, which was used in Ref. 10 (d_{min}=0.66 Å for the high-resolution bank and d_{min}=0.92 Å for the high-intensity bank), as compared to our Polaris data (d_{min}≈0.2 Å); the broader range used here is expected to yield more accurate ADPs. For the doped sample, the ADP values and their temperature trends were close to those in pure $BaZrO_3$.

Electron diffraction

We first discuss the electron diffraction data which provide the most direct evidence for the presence or absence of a superlattice. The ability to tilt the sample in a TEM at cryogenic temperatures is limited since tilting leads to temperature variations. With this limitation, we selected a single representative orientation along the ⟨310⟩ zone axis, which can reveal both *R*-type *½hkl* (*h*,*k*,*l*=odd) and *M*-type *½hk0* (*h*,*k*=odd) reflections expected for out-of-phase and in-phase octahedral rotations, respectively. The results for pure $BaZrO_3$ demonstrate conclusively the emergence of weak and diffuse, yet discrete, *R* spots below ≈80 K (Fig. 3a-d). The width of these reflections corresponds to a spherical domain size of about 3 nm to 4 nm, as estimated using Scherrer formula. The diffuse maxima at 1/3*hkl* positions which are present at all temperatures represent traces of truncation rods that arise because of the thin-foil geometry of a TEM sample, as has been additionally confirmed by tilting the sample and analyzing similarly oriented regions of different thicknesses at room temperature. The Nb-doped $BaZrO_3$ sample at ≈16 K also displayed the *R* spots (Fig. 3e), even though their intensity was much weaker compared to those in pure $BaZrO_3$. Yet, upon warming to ≈30 K, the superlattice spots grew stronger remaining visible up to ≈80 K, as in $BaZrO_3$ (Fig. 3f-h). The exact reasons for such in an irregular behavior of the *R*-spot intensities are unclear but can attributed to the effects of strain. Nevertheless, the doped sample appears to undergo the same symmetry lowering transition, although a quantitative comparison of the magnitudes of structural distortions in the two samples is precluded by the limited quality and scope of the present electron diffraction data (i.e., strong backgrounds, multiple-scattering effects, misorientations, *etc*.). Given the thin-foil nature of TEM samples, an ambiguity also remains about the observed superstructure being a bulk property. We addressed this latter question using structural refinements from the neutron total-scattering data, which also helped to confirm structural origins of the observed superlattice peaks.

Recovery of octahedral tilting from neutron total scattering

We established the feasibility of identifying nanoscale domains with weak octahedral rotations from neutron total scattering by performing RMC refinements using simulated data (Fig. 4). For this analysis, we created atomic configurations of $BaZrO_3$, 40 × 40 × 40 unit cells in size, that contained parallelepiped-shaped domains with side-dimensions of ≈3 nm, each featuring out-of-phase rotations of [ZrO_6] octahedra about one of the cubic axes; the rotation angle was set at 1.5 degrees. Thus, these domains exhibited $a^0a^0c^-$ [24] tilting, but the average symmetry of the resulting configuration was cubic. Additional random displacements, generated according to Gaussian distributions, were applied to Ba, Zr, and O to produce ADPs similar to those determined experimentally at 2 K. As expected, single-crystal diffuse-scattering patterns calculated for this model displayed the *R* reflections. Several such configurations were used to generate the simulated "experimental" *S*(*Q*), *D*(*r*), and Bragg profile. The feasibility tests were performed by refining atomic configurations of 20 × 20 × 20 cells against such simulated data under the polyhedral constraints. Fig. 4a illustrates the small difference between the *D*(*r*) curves simulated for the configuration with the tilted domains and those for the structure with the same ADP values but random oxygen displacements.

In the literature [24], the terms “octahedral rotations” and “octahedral tilting,” which are used interchangeably, usually implicitly assume correlated rotations of rigid octahedra, which, to maintain connectivity, form cogwheel patterns in the layers normal to the rotation axis. Rotations in successive layers along the rotation axis are unconstrained and can occur either in the same (in-phase) or opposite (out-of-phase) directions, giving rise to a variety of tilting patterns [24]. In structural snapshots, as deduced from total scattering, deformations of individual octahedra relative to the ideal arrangement reflect the superposition of various distortion modes, including rotations (e.g., see ref. 23, Supplemental information). Such rotations of the neighboring octahedra can be uncorrelated, with connectivity maintained by other types of octahedral distortions. In the context of the present study, we differentiate between uncorrelated and correlated/ordered octahedral rotations/tilts.

Fig. 4c and Fig. 4d compare spatial distributions of the *local* order parameter, η, which describes the degree of ordering for positive and negative octahedral rotations in the original (40 × 40 × 40) and refined (20 × 20 × 20) models. This parameter is defined as $\eta=(n_1-n_2)^2+(n_4-n_3)^2$, where n_i represents the fraction of those octahedra in the i^{th} coordination shell of the given octahedron that have the opposite sign of rotations relative to the central unit. That is, η=0 and η=2 correspond to disorder and perfect order, respectively. This parameter is calculated separately for every octahedron in a configuration and each tilting axis (*x*, *y*, *z*) so that a complete state of the rotational ordering is described by η_x, η_y, and η_z. The definition of the local-ordering metric adopted here has been previously used [22] to describe short-range rocksalt-type ordering. Indeed, for perfectly ordered out-of-phase tilting (e.g., the $a^0a^0c^-$ tilt system [24]), octahedra in alternating {111} lattice planes are rotated in opposite directions (Fig. 4b). As can be judged from Fig. 4d, which displays only those octahedra that have η_x, η_y, or η_z equal to 2, the refinements succeeded in reproducing the presence of the three nanoscale domain variants with $a^0a^0c^-$ rotations, although the fractions of these variants as well as the domain shapes deviated from those in the original model. The *R* spots in the diffuse scattering patterns were reproduced as well.

Another test involved data simulated for a model without tilting but having the same ADP values as the tilted array (the *D*(r) for this model is shown in Fig. 4a). Refining a 20 × 20 × 20 configuration against such data reproduced the disorder; expectedly, the corresponding single-crystal diffraction patterns contained no superlattice spots. The combined results of these tests indicate that error-free neutron total scattering data permit the recovery of the nanoscale octahedral tilting, if present.

Fits of the simulated data produced configurations with U_{ij} components of the ADP tensors that violated site symmetries expected for the *Pm-3m* space group beyond typical deviations in the 4th decimal place. These results indicate that in atomistic RMC refinements of structures with small ADPs, as encountered at cryogenic temperatures, neutron total scattering data, even if combined with a Bragg profile, are insufficient for constraining ADP components with adequate precision. Applying the ADP constraints described in the Experimental section addressed this issue while still permitting the recovery of the tilted domains, including the tilting patterns and rotation angles.

Atomistic refinements from experimental total neutron scattering

RMC refinements using the actual experimental data in all cases generated satisfactory fits (Fig. 5). The average atomic coordinates for the refined configurations were close to the ideal values for the corresponding Wyckoff positions in the *Pm-3m* structure. At 300 K, the components of the ADP tensors calculated from the atomic coordinates conformed to the expected site symmetries within typical

tolerances (±0.0002 Å^2). However, below 50 K, significant deviations were observed, as was encountered for the simulated data. At all temperatures and for all the species, the atomic probability density distributions could be described as Gaussians centered on the average crystallographic sites.

Diffuse scattering calculated for the refined configurations of $BaZrO_3$ at 2 K and 50 K exhibited discernable peaks at all the equivalent *R* and *M* points (Fig. 6a). At 300 K (Fig. 6b), no such spots were observed. Likewise, the superlattice peaks were absent for the Nb-doped $BaZrO_3$ (Fig. 6c) For the *R* spots, these results, therefore, agree with the electron diffraction data for $BaZrO_3$, but not for the doped sample. The *M* spots were not observed by electron diffraction.

We then repeated the refinements while constraining the ADPs to check whether the appearance of the diffuse spots at low temperatures could be linked to symmetry-breaking for the ADP components, as observed in the unconstrained refinements. We tried both versions of the ADP restraints and obtained similar-quality fits. Importantly, the presence or absence of the diffuse *R* and *M* reflections was reproduced regardless of constraints. Given only a small difference between the total-scattering signals from pure and Nb-doped $BaZrO_3$, two additional tests were performed. In one case we used a refined model for the pure structure, which yields the superlattice spots, and continued its refinement against the experimental data for the Nb-doped sample. In another test, we performed a similar exercise but refined the model for Nb-doped $BaZrO_3$ at 2 K against the same temperature data for the pure structure. In both cases, using the model from the chemically different sample resulted in significantly worse (factor of ≈1.5) initial values of the fitting metrics. In the first test, the superlattice reflections, which were present at the start, gradually disappeared after the fit, whereas in the second test, the opposite results were obtained. We therefore concluded that the correlations among atomic displacements, which are the origin of these spots, are required by the neutron data.

The refined configuration for $BaZrO_3$ at 2 K displays a visually identifiable preference for a chess-board pattern of clockwise and counter-clockwise octahedral rotations in the plane perpendicular to the rotation axis (Fig. 7a). For adjacent octahedral chains along the rotation axis, the rotations occur preferentially out of phase, providing a further indication of cogwheel-like tilts in multiple octahedral layers (Fig. 7b). We quantified the state of the rotational ordering by introducing a Warren-Cowley "in-plane" order parameter, $\alpha(i)$, defined as $\alpha(i)=(p(i)-0.5/0.5)$, where *i* is the number of the coordination shell around the given "reference" octahedron in the plane perpendicular to the rotation axis, and $p(i)$ is the probability of finding an octahedron (in the i^{th} coordination shell) rotated in the direction opposite to that of the reference. Compared to η, the α-parameter emphasizes the existence and spatial extent of a cogwheel pattern of rotations in the layers perpendicular to the rotation axis, which, as mentioned above, is the most fundamental indicator of rotational ordering for rigid octahedra, regardless of relations among octahedral tilts in successive layers along the rotation axis. Fig. 8 displays $\alpha(i)$ values calculated for octahedral sheets normal to the rotation axis for the $BaZrO_3$ configurations at 2 K and 300 K. At both temperatures, the nearest-neighbor octahedra are preferentially rotated out of phase. However, at 300 K, the order parameter becomes close to zero for the next-nearest neighbors, whereas at 2 K, the cogwheel-like order (Fig. 8) is maintained over extended distances. A similarly defined Warren-Cowley order parameter for rotations of the nearest-neighbor octahedra in the chains along the rotation axis is equal to ≈0 and ≈0.2 at 300 K and 2 K, respectively, indicating a preference for out-of-phase tilts in successive layers at low temperatures. A given refined configuration featured pronounced ordering of tilts around a single axis, (i.e., *x*, *y*, or *z*) rather than an assemblage of nanoscale domains, each having a

unique rotation axis. A map of the η_X order parameter is displayed in Fig. 8c, revealing regions with a significant degree of $a^0a^0c^-$-type ordering that span a large part of the configuration; for the same configuration, the η_Y and η_Z distributions (not shown) display no clustering of octahedra, which indicates the absence of extended ordering for tilts around these axes.

Further analysis of the diffuse scattering for the RMC-refined configurations revealed that the *R* and *M* reflections arise primarily from oxygen and cation displacements, respectively (Fig. 9). For oxygen, a condensation of the diffuse intensity at the *M*-spot locations is attributed to regions with a preference for in-phase tilts along the tilting axis (Fig. 9), which is inevitable for partly disordered rotations. Such weak diffuse scattering could be difficult to detect by electron diffraction, especially in the presence of a relatively strong background. In contrast, the cations yield much stronger discrete *M*-spots. The diffuse *M*-spots have been observed previously by electron diffraction in several Pb-based perovskites and attributed to anti-parallel cation displacements [25, 26], though their exact origins remained debatable. In the present case, given the relatively small ionic polarizabilities of Zr and Ba together with the absence of the *M*-spots in our electron diffraction patterns, which are expected to be sensitive to such heavy species, we considered correlated cation displacements giving rise to the *M* reflections as an artifact of the RMC refinements. Indeed, because of the strong overlap between the cation-cation and cation-oxygen partial PDFs, cation displacements are likely to compensate the effects of oxygen-oxygen correlations on the data.

We used the inverse Fourier transform (IFT) of the scattering amplitude for the *R*-spots, calculated in the vicinity of the oxygen positions, to identify correlations among atomic displacements that give rise to these superlattice reflections. The IFT of diffuse scattering yields positive maxima around the atomic positions included in the calculations. A separate study [23] using computer-simulated structures demonstrated that for such IFT peaks with the strongest intensity, vectors joining the average atomic positions and locations of the positive peaks represent components of atomic displacements that contribute to the diffuse scattering in question. Such a method, albeit computationally intensive, provides a way to unambiguously link specific diffuse-scattering features to the underlying atomic displacements. Here, for the IFT of the *R*-spots, we selected oxygen atoms with the largest values of the transform and considered rotations of [ZrO_6] octahedra containing these atoms (Fig. 10). These octahedra form dense three-dimensional clusters, 2 nm to 3 nm in size, featuring a cogwheel pattern of positive and negative rotations in the planes perpendicular to the rotation axis, and a preference for out-of-phase rotations along that axis.

Summary

Our electron-diffraction and atomistic-refinement results converge on the existence of correlated octahedral rotations in bulk $BaZrO_3$ below 80 K. These rotations occur preferentially out-of-phase and the observed tilting pattern resembles the $a^0a^0c^-$ type, which has been suggested by theoretical calculations as well as the high-pressure structure of BaZrO3 [27], and a phase diagram for (Ba,Ca)ZrO_3 solid solutions [28]. The rotation angles in the regions of stronger order are between 2° and 3°. The emergence of relatively sharp superlattice reflections below a certain temperature resembles a phase transition more than dynamic correlations, even though the present measurements are insufficient to unambiguously resolve these scenarios. In $BaZrO_3$, quantum effects reportedly also become significant below 80 K [8]. Therefore, a picture of zero-point fluctuations limiting the coherence length for the octahedral rotations and preventing the establishment of macroscopic order is plausible. The inability of

the structural refinements to reproduce correlated rotations in the Nb-doped case, which are revealed by electron diffraction data, can be attributed to a weaker magnitude of the correlated tilting compared to the pure compound. Such weaker distortions could be linked to the smaller ionic radius of Nb^{5+} as compared to Zr^{4+} and/or also to larger quantum effects for the doped sample, as suggested by the lattice-parameter trends.

Conclusions

Electron diffraction has demonstrated the occurrence of a structural change in $BaZrO_3$ below 80 K, which is evidenced by the appearance of *½hkl* (*h*, *k*, *l*=odd) superlattice reflections. Large-box refinements from the neutron total-scattering data using the RMC method confirmed this change to be a bulk effect associated with the onset of nanoscale correlations of octahedral rotations. The rotations are of the $a^0a^0c^-$-type, with the size of strongly ordered regions about 3 nm. Nb-doped $BaZrO_3$ undergoes a similar structural change, as indicated by the emergence of the superlattice spots, but in this case, the distortions appear to be weaker than in the pure compound. The evidence presented here supports theoretical predictions of a tilting instability in $BaZrO_3$ associated with the so-called R_{25} vibrational mode that represents out-of-phase octahedral rotations, even though we cannot conclusively discern between static and dynamic effects. Our results are also consistent with proposals that zero-point quantum fluctuations limit the correlation length for the octahedral rotations and prevent a macroscopic phase change. The development of the tilted superstructure in both pure and Nb-doped samples suggest that the low-temperature dielectric anomaly previously attributed to the onset of octahedral rotations is caused by other effects, since it disappears upon doping. Further reconciliation of various density-functional-theory treatments as well as reassessment of interpretations of spectroscopic (optical, dielectric) data for $BaZrO_3$ are needed.

Acknowledgements

We thank the STFC (UK) for access to the ISIS neutron facility and R. Smith for technical assistance with the data collection. We are also grateful to M. Eremenko (Skoltech) for his help with the scripts for simulating structural models and visualizing the results. The work at the Brookhaven National Laboratory was supported by Materials Science and Engineering Division, Office of Basic Energy Science of the U.S. Department of Energy under contract no. DESC0012704.

References

1. H. D. Megaw, Proc. Phys. Soc., 58, 133 (1946)
2. H. Tamura, T. Konoike, Y. Sakabe, K. Wakino, J. Am. Ceram. Soc., 67 [4] (1984)
3. L. Zhang, Y. P. Pu, M. Chen, J. Alloys Compounds, 775, 342 (2019)
4. M. H. Zhang, K. Wang, Y. J. Du, G. Dai, W. Sun, G. Li, D. Hu, H. C. Thong, C. Zhao, X. Q. Xi, Z. X. Yue, J. F. Li, J. Am. Chem. Soc., 139 [10] 3889 (2017)
5. L. Dong, D. S. Stone, R. S. Lakes, J. Appl. Phys., 111 [8] 084107 (2012)
6. Y. Yamazaki, F. Blanc, Y. Okuyama, L. Buannic, J. C. Lucio-Vega, C. P. Grey, Nature Mater., 12, 647-651 (2013)
7. H. K. Dai, H. N. Kou, H. Q. Wang, K. Bi, Electrochem. Comm., 96, 11 (2018)
8. A. R. Akbarzadeh, I. Kornev, C. Malibert, L. Bellaiche, J. M. Kiat, Phys. Rev. B., 72, 205104 (2005)
9. A. Perrichon, E. J. Granhed, G. Romanelli, A. Piovano, A. Lindman, P. Hydgaard, G. Wahnstrom, and M. Karlsson, Chem. Mater., 32 [7], 2824 (2020)
10. K. S. Knight, J. Mater. Sci., 55, 6417 (2020)
11. J. C. Bennett, I. Grinberg, A. M. Rappe, Phys. Rev. B., 73, 180102 (2006)
12. A. Bilic, J. D. Gale, Phys. Rev. B., 79, 174107 (2009)
13. A. I. Lebedev and I. A. Sluchinskaya, Phys. Solid State, 55, 1941 (2013)
14. C. Toulouse, D. Amoroso, C. Xin, Ph. Veber, M. C. Hatnean, G. Balakrishnan, M. Maglione, Ph. Ghosez, J. Kreisel, M. Guennou, Phys. Rev. B., 100, 134102 (2019)
15. T. Kolodiazgnyi, P. Pulphol, W. Vittayakorn, N. Vittaykorn, J. Eur. Ceram. Soc., 39 [14] 4144 (2019)
16. R. D. Shannon, Acta Cryst. A., 32, 751 (1976)
17. A. C. Larson, R. B. V. Von Dreele. GSAS. Report LAUR 86-748, Los Alamos National Laboratory, New Mexico, USA
18. M. G. Tucker, D. A. Keen, M. T. Dove, A. L. Goodwin, Q. Hui, J. Phys. Cond. Matter, 19, 335218 (2007)
19. M. Eremenko, V. Krayzman, A. Gagin, I. Levin, J. Appl. Cryst., 50, 1561 (2017)
20. Y. Zhang, M. Eremenko, V. Krayzman, M. G. Tucker, I. Levin, J. Appl. Cryst., 53[6] 1509 (2020)
21. H. Y. Playford, L. R. Owen, I. Levin, M. G. Tucker, Annu. Rev., Mater. Res. 44, 429 (2014)
22. S. Wells, A. Sartbaeva, Mol. Simul. 41 1409 (2015)
23. M. Eremenko, V. Krayzman, A. Bosak, H. Y. Playford, K. W. Chapman, J. C. Woicik, B. Ravel, I. Levin, Nat. Comm., 10(1), 2728 (2019)
24. A. M. Glazer, Acta Crystallogr., B., 28, 3384 (1972)
25. R. E. Eitel, S. J. Zhang, T. R. Shrout, C. A. Randall, I. Levin, J. Appl. Phys.., 96 [5] 2828 (2004)
26. D. L. Corker, A. M. Glazer, R. W. Whatmore, A. Stallard, F. Fauth, J. Phys. Condens. Matter 10, 6251 (1998)
27. X. Yang, Q. Li, R. Liu, B. Liu, H. Zhang, S. Jiang, J. Liu, B. Zou, T. Cui, B. Liu, J. Appl. Phys, 115 [12] 124907 (2014)
28. I. Levin, T. G. Amos, S. M. Bell, L. Farber, T. A. Vanderah, R. S. Roth, B. H. Toby, J. Solid State Chem., 175 [2], 170 (2003)
29.

M. A. Helal, S. Kojima, Mater. Sci & Eng B, B271, 115314 (2021)

J. Zhang, Y. Zhang, T. Xu, J. Wang, Phys. Rev. B., 103, 014113 (2021)

Figure captions

Fig. 1: Comparison of experimental neutron *D*(r) for (a, b) $BaZrO_3$ at 2 K (black) and 50 K (red) and for (d, e) $BaZrO_3$ (black) and $BaZr_{0.995}Nb_{0.005}O_3$ (red) at 2 K, after accounting for the *r*-shifts associated with small differences in the lattice parameters of the two samples. The red and black traces are close and difficult to differentiate in the figure. The corresponding residual traces are shown in green. Figs. 1c and 1e compare these residuals (green) with the statistical noise (magenta) estimated from the standard deviations in the measured scattered intensities; the differences are small but significant.

Fig. 2: (a) Lattice parameters of $BaZrO_3$ and $BaZr_{0.995}Nb_{0.005}O_3$ as a function of temperature. The uncertainties (a single standard deviation) are within the symbol size but can also be assessed from the consistency of the respective trends. The divergence of the trends below 100 K is significant with respect to these uncertainties. (b-c) Refined values of the APDs for oxygen (anisotropic) and the cations (Ba, Zr, isotropic). $BaZr_{0.995}Nb_{0.005}O_3$ exhibited similar trends for the ADPs (not shown).

Fig. 3: Selected area electron diffraction patterns of (310) zone axis recorded from single grains in the $BaZrO_3$ (a-d) and $BaZr_{0.995}Nb_{0.005}O_3$ (e-h) samples at 16 K, 47 K, 60 K, and 300 K. The contrast in the rectangular band around the ½*hkl* (*h*,*k*,*l*=odd) spots (circled in red) in the upper portions of these patterns has been enhanced using an image-processing software to improve their visibility. The appearance of these spots as recorded can be seen from the lower portions of the patterns.

Fig. 4: (a) Comparison of *D*(r)s calculated for the simulated models of $BaZrO_3$ with (black) and without (red) the tilted domains, both having the same ADP values. (b) A schematic drawing of the perovskite structure with $a^0a^0c^-$ tilting of the oxygen octahedra. The directions of rotations are indicated using both red arrows and distinct colors to highlight the similarity between such a pattern of rotations and the rocksalt-type ordering of octahedral species; this similarity has been used to define the local order parameter for octahedral rotations. The numbers in this figure (from 1 to 4) mark the octahedra forming the four successive coordination spheres around the central octahedron labelled with "0", which have been used for calculating the local order parameter η (see text). (c-d) spheres representing those octahedra in the model (c) and (d) refined configurations that acquired the maximum value of η=2. Different colors refer to η_x, η_y, and η_z. Clusters of spheres of the same color represent nanoscale domains with $a^0a^0c^-$ rotations about *x* (red), *y* (green), and *z* (blue) axes. Axis units correspond to the number of unit cells in the configuration. Note that the side-length of the refined configuration (d) is half that of for the original model (c) which was used to generate the simulated experimental data (a).

Fig. 5: Experimental (black) and calculated (red) (a, b) *D*(*r*), (c) *F*(*Q*), and (d) Bragg profile for $BaZrO_3$ at room temperature. The calculated signals correspond to the refined atomic configurations. The difference traces are shown in green. Similar quality fits were obtained for other temperatures as well as for $BaZr_{0.995}Nb_{0.005}O_3$.

Fig. 6: {301} sections of reciprocal-space with calculated X-ray diffuse scattering for the RMC-refined configurations of $BaZrO_3$ at 2 K (a) and 300 K (b), and of $BaZr_{0.995}Nb_{0.005}O_3$ at 2 K (c). Here, the term "diffuse scattering" refers to any scattering other than the Bragg reflections determined by the

average perovskite unit cell. The *R* and *M* spots (labelled in Fig. 5a) are observed for $BaZrO_3$ at 2 K, but not for the Nb-doped sample. For $BaZrO_3$, these spots persist at 50 K (not shown) but disappear at 300 K.

Fig. 7: (a) A representative {*yz*} layer of the refined configuration for $BaZrO_3$ at 2 K. Squares symbolize [ZrO_6] octahedra with the color scale encoding their rotation angles around the *x*-axis. The blue and red colors correspond to the negative and positive signs of rotations, respectively. The presence of extended regions with chess-board patterns of positive and negative rotations is evident. (b) Rotation angle as a function of the octahedron's number along the two adjacent octahedral chains (encircled in (a)) parallel to the *x*-axis. The rotations in the two neighboring chains occur preferentially out of phase with each other, which indicates that the *in-plane* order of rotations is maintained in multiple {*yz*} layers.

Fig. 8: (a) Dependence of the *in-plane* order parameter $\alpha(n)$ on the number of the coordination sphere, *n*, for the neighboring octahedra (as illustrated using a schematic drawing in Fig. 8b) for the refined configurations of $BaZrO_3$ at 2 K (black) and 300 K (red). At 300 K, $\alpha(n)$ becomes nearly zero already for *n*=2, whereas at 2 K it persists to much larger distances consistent with Fig. 7. (c) A 3D distribution of the local tilting order parameter η_x (see text) in a refined configuration of $BaZrO_3$ visualized using isosurfaces. The top-right octant has been cut out to reveal that internal regions exhibit higher (>1) values of η. The color scale bar represents values of η. This map illustrates that regions with significant degree of rotational ordering (η>0.5) represent a large part of the configuration.

Fig. 9: {310} sections of reciprocal space with calculated X-ray diffuse scattering for a refined configuration of $BaZrO_3$ at 2 K using (a) oxygen atoms, (b) Zr and Ba, (c) all species. The *R*-spots apparently arise exclusively from oxygen whereas the *M*-spot intensities are dominated by the cations with small contributions from oxygen.

Fig. 10: A subset of of the [ZrO_6] octahedra, represented using spheres, in the refined configuration of $BaZrO_3$ at 2 K, containing those oxygen atoms that provide the largest contribution to the *R*-spot intensities in the calculated diffuse scattering (Fig. 6) as revealed using the IFT of these reflections. The color scale reflects the rotation angles of the corresponding octahedra around the *x*-axis (horizontal). These octahedra form dense clusters, several nanometers in size, one of which is depicted in this figure. Inside such clusters, in the planes perpendicular to the tilting axis, the red and blue spheres can be seen preferentially forming a chess-board pattern as expected for the tilting of rigid octahedra. Along the rotation axis, there is a preference for alternating positive and negative rotations as also confirmed by calculating the relevant probabilities.

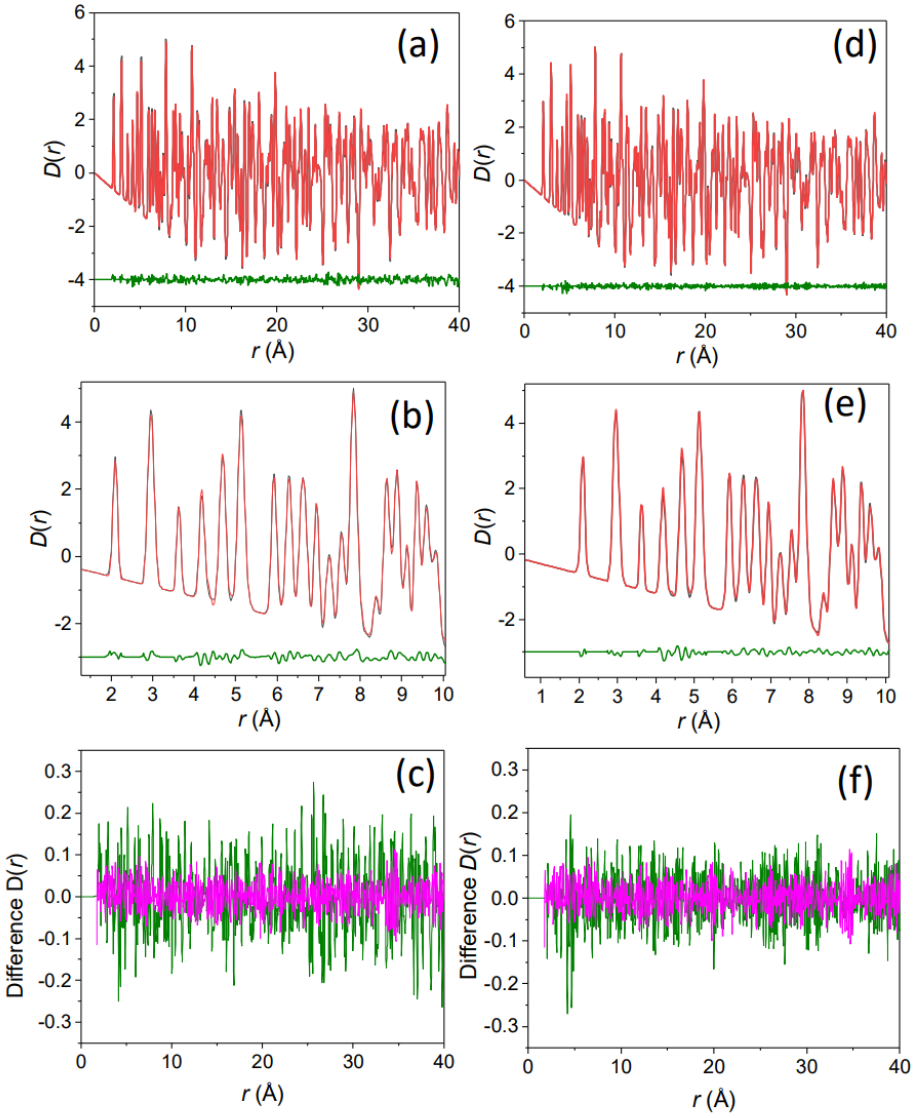

Fig. 1

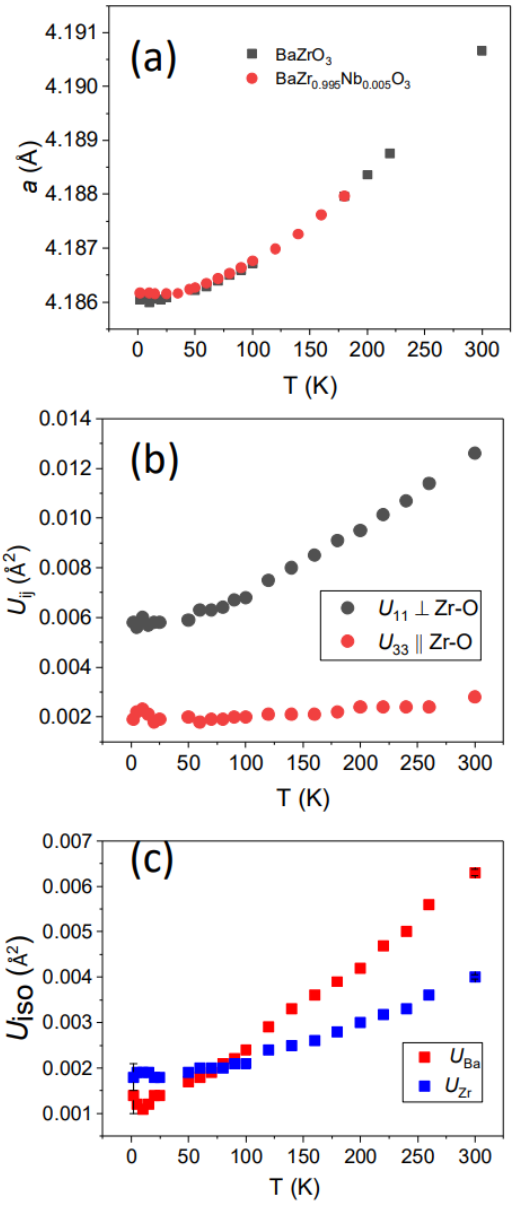
(a)
BaZrO3
BaZr0.995Nb0.005O3
a (Å)
4.191
4.190
4.189
4.188
4.187
4.186
0
50
100
150
200
250
300
T (K)
(b)
Uij (Å2)
0.014
0.012
0.010
0.008
0.006
0.004
0.002
U11 ⊥ Zr-O
U33 ∥ Zr-O
T (K)
(c)
Uiso (Å2)
0.007
0.006
0.005
0.004
0.003
0.002
0.001
UBa
UZr
T (K)

Fig. 2

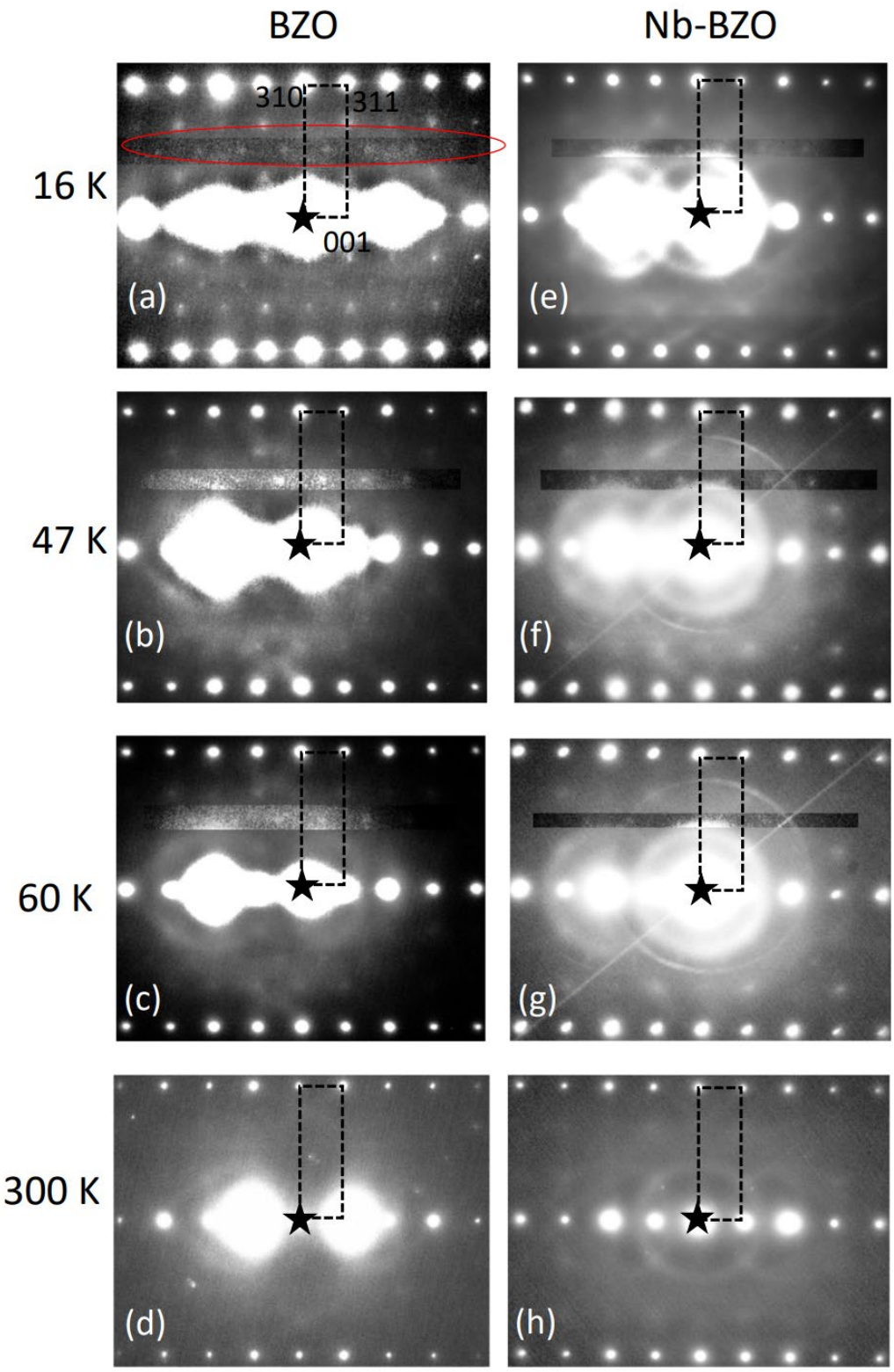

Fig. 3

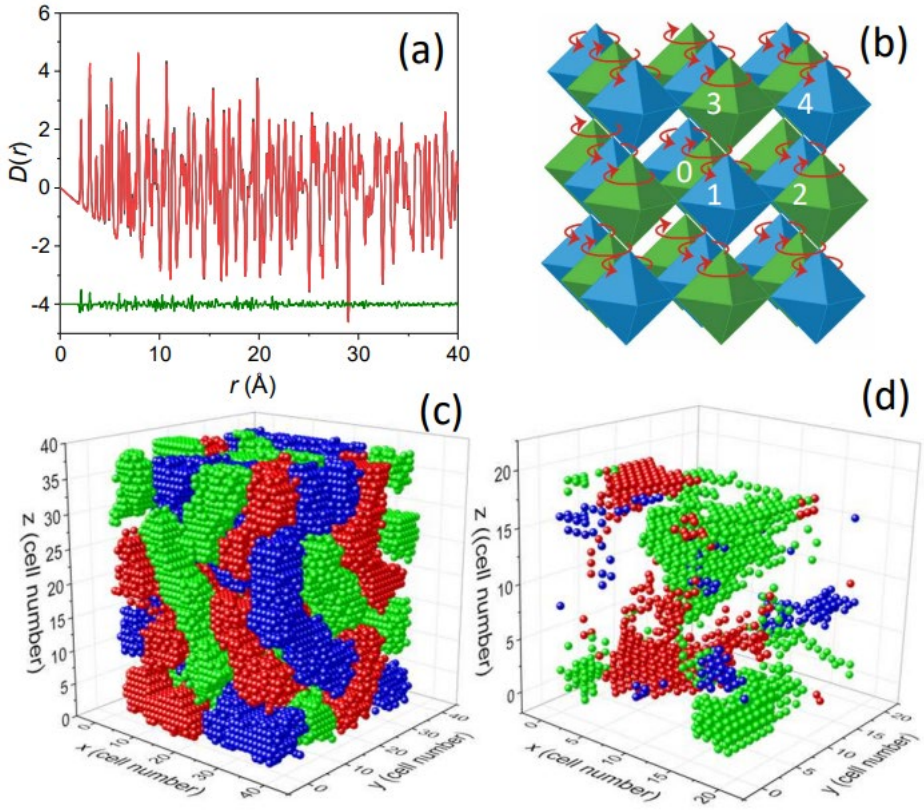
(a)
D(r)
r (Å)
(b)
0
1
2
3
4
(c)
z (cell number)
x (cell number)
y (cell number)
(d)
z ((cell number)
x (cell number)
y (cell number)

Fig. 4

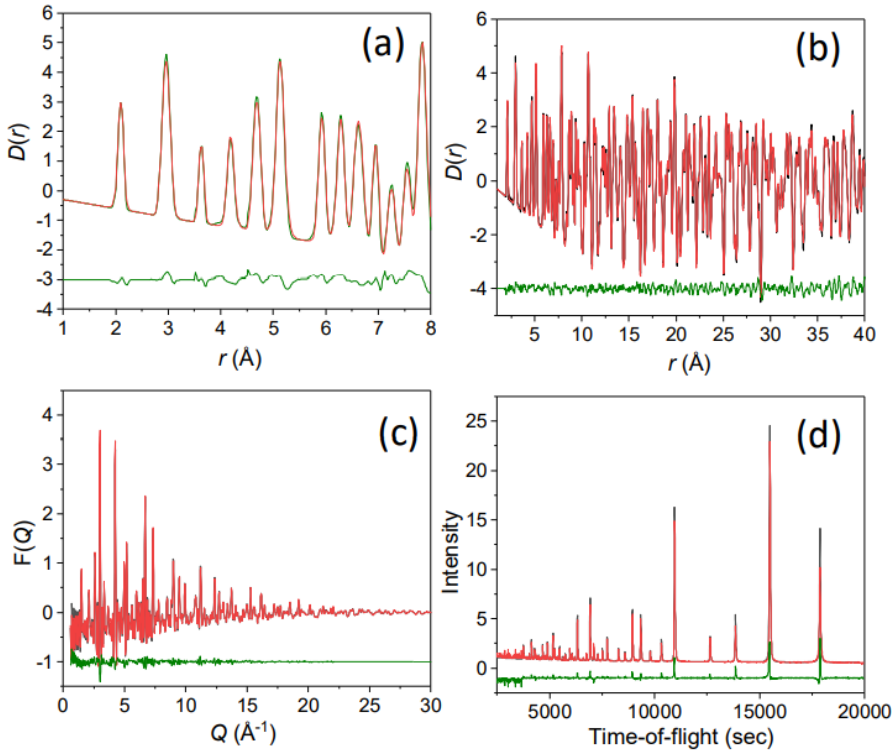

Fig. 5

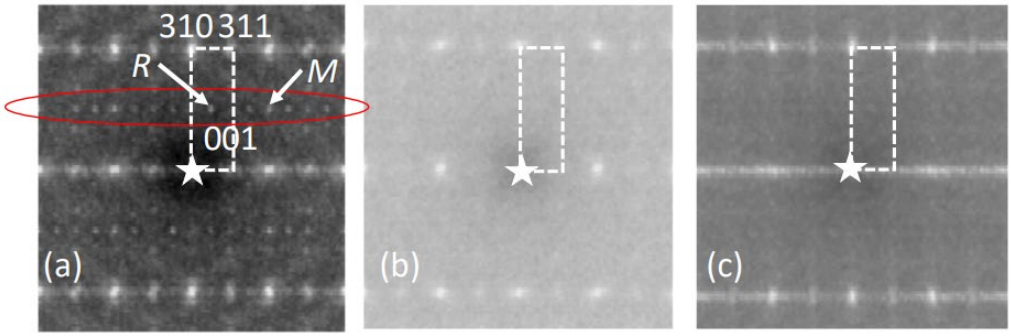

Fig. 6

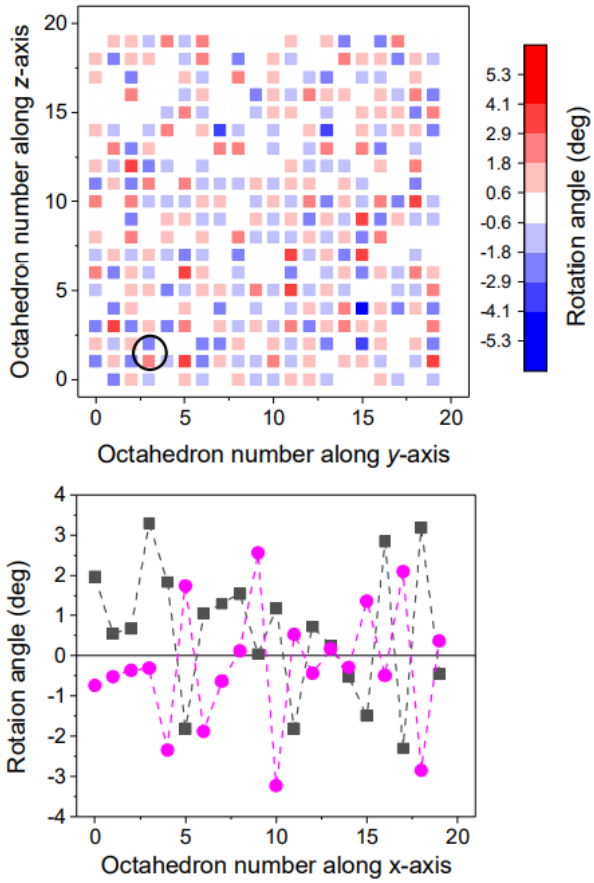
Octahedron number along z-axis
Octahedron number along y-axis
Rotation angle (deg)
5.3
4.1
2.9
1.8
0.6
-0.6
-1.8
-2.9
-4.1
-5.3
Rotaion angle (deg)
Octahedron number along x-axis

Fig. 7

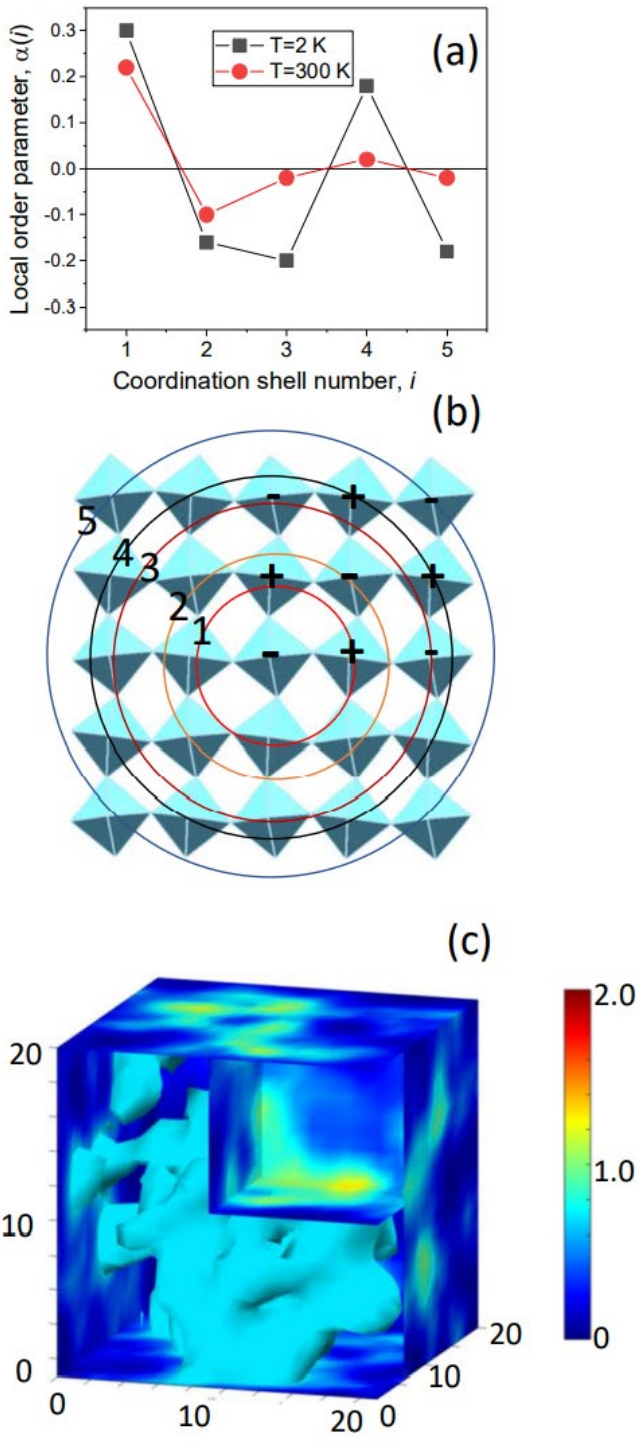
(a)
T=2 K
T=300 K
Local order parameter, α(i)
Coordination shell number, i
(b)
5
4
3
2
1
(c)
2.0
1.0
0
20
10
0

Fig. 8

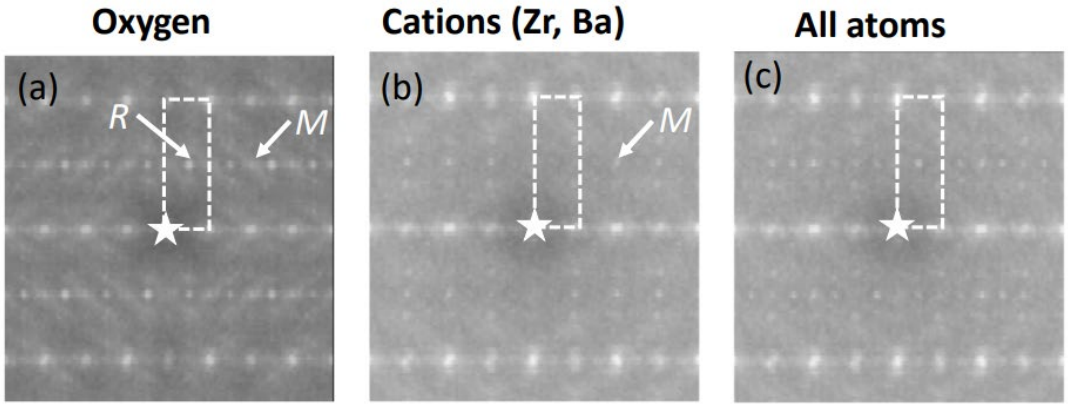

Fig. 9

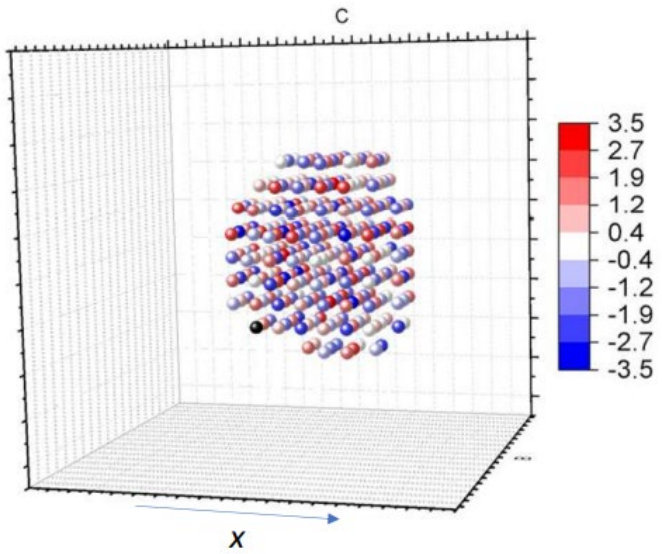

Fig. 10